PCCP

PAPER

Cite this: *Phys. Chem. Chem. Phys.*, 2014, **16**, 18866

Efficient C–C bond splitting on Pt monolayer and sub-monolayer catalysts during ethanol electro-oxidation: Pt layer strain and morphology effects†

Rameshwori Loukrakpam,[a] Qiuyi Yuan,[b] Valeri Petkov,[c] Lin Gan,[a] Stefan Rudi,[a] Ruizhi Yang,[d] Yunhui Huang,[e] Stanko R. Brankovic[b] and Peter Strasser*[a]

Received 25th June 2014,
Accepted 21st July 2014

DOI: 10.1039/c4cp02791d

www.rsc.org/pccp

Efficient catalytic C–C bond splitting coupled with complete 12-electron oxidation of the ethanol molecule to CO_2 is reported on nanoscale electrocatalysts comprised of a Pt monolayer (ML) and sub-monolayer (sML) deposited on Au nanoparticles (Au@Pt ML/sML). The Au@Pt electrocatalysts were synthesized using surface limited redox replacement (SLRR) of an underpotentially deposited (UPD) Cu monolayer in an electrochemical cell reactor. Au@Pt ML showed improved catalytic activity for ethanol oxidation reaction (EOR) and, unlike their Pt bulk and Pt sML counterparts, was able to generate CO_2 at very low electrode potentials owing to efficient C–C bond splitting. To explain this, we explore the hypothesis that competing strain effects due to the Pt layer coverage/morphology (compressive) and the Pt–Au lattice mismatch (tensile) control surface chemisorption and overall activity. Control experiments on well-defined model Pt monolayer systems are carried out involving a wide array of methods such as high-energy X-ray diffraction, pair-distribution function (PDF) analysis, *in situ* electrochemical FTIR spectroscopy, and *in situ* scanning tunneling microscopy. The vibrational fingerprints of adsorbed CO provide compelling evidence on the relation between surface bond strength, layer strain and morphology, and catalytic activity.

1. Introduction

Ethanol is known to have high energy density as a fuel in direct alcohol polymer electrolyte fuel cells. Major problems associated with the development of electrocatalysts for ethanol oxidation are (i) the high content of Pt in conventional catalysts limiting the cost-efficacy of the catalysts, and (ii) the incomplete oxidation of ethanol with high selectivity toward acetaldehyde and acetic acid instead of carbon dioxide.[1] Despite extensive work on ethanol oxidation catalysts, it has been difficult to catalyze the ethanol adsorption and subsequent C–C bond splitting at relevant potentials without Pt as a main constituent of the catalyst. Some of the methods in which Pt content can be lowered are by using advanced nano-structural materials such as nanoparticles with core–shell structures,[2,3] Pt monolayers catalyst[4] and 2D nanostructures.[5,6] Alternatively, alloying of Pt with other non-noble metals to form binary or ternary alloys has been shown as promising strategies.[2,7,8] The merit criteria when designing the catalyst for EOR is its ability to alleviate formation of undesired by-products like acetic acid or acetaldehyde, according to

$$CH_3CH_2OH \rightarrow CH_3CHO + 2H^+ + 2e^-$$

$$CH_3CHO + H_2O \rightarrow CH_3COOH + 2H^+ + 2e^-$$

which reduces the faradaic efficiency of the anodic reaction of direct ethanol fuel cells (DEFCs). In particular, the formation of acetic acid and subsequent poisoning of the actives sites is a major undesirable reaction pathway. Therefore, a desired catalyst for EOR would facilitate the complete ethanol oxidation *via* the 12 electron oxidation pathway with the production of CO_2 according to

$$CH_3CH_2OH + 3H_2O \rightarrow 2CO_2 + 12H^+ + 12e^-$$

which requires the splitting of the C–C along the reaction pathway.

In literature, there have been previous attempts to use Pt ML structures for catalytic surface reactions. Most of these Pt MLs have been prepared using surface limited redox replacement

[a] *Department of Chemistry, Chemical Engineering Division, Technical University Berlin, Berlin 10623, Germany. E-mail: pstrasser@tu-berlin.de*
[b] *Department of Electrical and Computer Engineering, University of Houston, Houston, TX 77204, USA*
[c] *Department of Physics, Central Michigan University, Mt. Pleasant, MI 48859, USA*
[d] *School of Energy, Soochow University, Suzhou, Jiangsu 215006, China*
[e] *College of Materials Science and Engineering, Huazhong University of Science and Technology, Wuhan, 430074, China*

† Electronic supplementary information (ESI) available. See DOI: 10.1039/c4cp02791d

(SLRR) of UPD MLs, also known as the galvanic displacement method, on well-defined single crystal surfaces.[9] The amount of deposited metal was defined by stoichiometry of the redox reaction and structure of the UPD metal adlayer.[10] Morphology of the Pt deposit was found to be dependent on UPD ML coverage, and reaction kinetics parameters defined by conditions of the deposition experiment.[11,12] Li *et al.* reported both methanol and ethanol oxidation reactions on Pt ML/Au(111), which was prepared using SLRR.[13] It was found that such well-defined extended (macroscopic) Pt MLs were active for the anodic oxidation of both methanol and ethanol. CO_2 formation was observed in methanol oxidation on Pt ML/Au(111) using *in situ* FTIR studies. However, no CO_2 peak was recorded in case of ethanol oxidation on these catalytic surfaces. High EOR activity on Pt ML/Au(111) was reported to be due to the fast kinetics of reaction pathway generating acetic acid and acetaldehyde only.

The coherent strain in an ideal continuous metal ML catalyst is directly dependent on the epitaxial relation and misfit between the catalyst material and substrate. In continuous Pt ML on Au(111), Pt atoms retain the same in-plane inter-atomic distance as Au atoms and the misfit in the lattice parameters gives a positive coherent (tensile) strain in Pt monolayer ($\sim$4%). According to the d-band model,[14] for a substrate with weak electronic effect such as gold, the tensile strain leads to a shift in the energy of Pt d-band center towards Fermi level resulting in increased reactivity. However, in factual conditions, catalyst morphology of Pt ML and sML resembles 2D clusters rather than a continuous monolayer. Recent studies on single crystal Au substrates show that in 2D Pt nanocluster configuration the resulting active strain in 2D nanoclusters represents the convolution of the *tensile strain (expansive) due to the epitaxial misfit* and the *compressive strain due to the finite size effects*. This results in the situation where the activity of Pt ML and sML on Au(*hkl*) is mainly the function of their morphology/size with overall trend showing a higher activity as compared to the bulk Pt(111).[12]

In this report, we study the surface catalytic effect of Pt MLs and Pt sMLs on Au nanoparticles (NPs) aimed for applications in DEFCs as anodic ethanol oxidation catalyst. SLRR of Cu UPD ML is used to synthesize and prepare the Au@Pt ML and Au@Pt sML catalysts in an industrial scaled-up batch reactor which has direct relevance for synthesis of the electrocatalyst for real commercial applications. It was found that Pt ML and sML on Au NPs were able to induce complete dehydrogenation of ethanol *via* C–C bond splitting with the Pt ML giving better catalytic activity and more efficient earlier on-set potential of CO_2 production.

2. Experimental section

2.1 Chemicals and materials synthesis

40% Au nanoparticles on Vulcan XC-72 carbon was purchased from Premetek Co., copper(II) sulphate pentahydrate from Alfa Aesar, potassium tetrachloroplatinate(II), potassium hexachloroplatinate(IV) and Nafion® (5% by wt and 20% by wt) were obtained from Sigma Aldrich. Sulfuric acid (AnalaR NORMAPUR@ACS, 95%), absolute ethanol (Commercial Alcohols Inc., 100% ACS grade) and ultrapure water (18 MΩ cm. Millipore) were used to prepare the solutions for the electrochemical testing. Ultra-high purity sulfuric acid and perchloric acid were used for the electrochemical synthesis and FTIR. All the other solvents were of analytical grade and were used without further purification.

Synthesis of Au@Pt ML and Au@Pt sML. A scale-up electrochemical synthesis method was used to prepare Au@Pt ML and Pt Au@Pt sML electrocatalysts. Similar scale up protocols for electrochemical synthesis has been reported by Sasaki *et al.*[15] A custom-built cell was used with graphite sheet as working electrode and SCE (+0.323 V *vs.* RHE) electrode as reference and a Pt wire as counter electrode. 100 mg of commercial supported Au NPs (metal loading 40%) from Premetek Inc., was placed at the bottom of the cell in contact with the graphite sheet. 50 ml of 0.05 M H_2SO_4 was used as the electrolyte. The chamber was deaerated while stirring for 1 h and then, left at rest for 30 minute to allow for the sample to come in contact with the graphite sheet for better electrical contact. Initial cleaning cyclic voltammetric scans for 50 cycles was run from 0.22 V to 1.27 V *vs.* RHE at 50 mV s^{-1} scan rate to clean the surface of the catalyst of any residue. Deaerated 0.35 M $CuSO_4{\cdot}5H_2O$ was added to the experimental chamber and Cu(II) UPD deposition at 0.33 V was performed for 3 h. After Cu UPD deposition was completed, 6 mM solution of K_2PtCl_4 solution (or 3 mM solution of K_4PtCl_6 solution) was added drop-wise and stirred for 1.5 hours to allow spontaneous displacement of Cu^{2+} by Pt^{2+} or Pt^{4+}. The solution was centrifuged and washed multiple times with deionized water and then freeze dried.

Preparation of supported Pt NPs. Supported Pt NPs nanoparticles were prepared using a modified polyol synthesis reported in literature.[6] Pt precursor was reduced using 1,2-hexadecanediol in the presence of oleic acid and oleylamine in dioctylether solvent at 200 °C. The nanoparticles are then supported on Vulcan XC-70 carbon black and thermally treated in a quartz tube furnace.

Catalyst ink preparation for electrochemical testing. A typical catalyst ink preparation involved the following steps: 9 mg of the electrocatalyst was taken with 5 ml of deionized water, 1 ml of isopropanol and 40 μL of 5% Nafion. The mixture was sonicated for 2 hour in an ice bath to form a uniform catalysts ink. Glassy carbon (GC) electrode was polished in 0.05 μm Alumina and then sonicated in deionized water. The electrode was finally rinsed with deionized water and dried. 20 μL of the ink was pipette on the GC electrode (geometric area: 0.196 cm^2) and dried giving a catalysts loading of 153 μg cm^{-2}. This GC electrode was used for electrochemical testing experiments of these electrocatalysts.

Catalyst ink preparation for *in situ* FTIR. A typical catalyst ink preparation involved the following steps: 10 mg of the electrocatalyst was taken with 8 ml of de-ionized water, 2 ml of isopropanol and 80 μL of 20% Nafion. The mixture was sonicated for 2 hour in a water bath to form a uniform catalysts ink. Au(100) single crystal was polished and rinsed with deionized water and dried. The ink was pipette on the Au crystal and dried to give a uniform layer for FTIR studies.

2.2 Characterization and electrochemical measurements

Transmission electron microscopy (TEM) and energy dispersive X-ray spectroscopy (EDX) was used to study morphology

and composition. A small amount of the electrocatalysts was dispersed *via* ultrasonication in 0.5 ml hexane. A Cu-grid coated with holey carbon film was impregnated with 2 μl of the solution and air-dried. A FEI TECNAI G^2 20 S-TWIN microscope, equipped with a GATAN MS794 P CCD-detector operated at 200 kV was used. The mean particle size was determined from the TEM images by counting of 50–200 particles. EDX data were collected for 120 s at an angle of 45° with respect to the sample holder.

High-energy synchrotron X-ray diffraction (HEXRD) measurements were performed at the beam line 11-ID-C, at the Advanced Photon Source, Argonne National Laboratory using X-rays of energy ~115 keV corresponding to wavelength of 0.1080 Å. For the measurements small amounts of commercial supported Au, supported Pt NPs, Au@Pt ML and Au@Pt sML nanoparticles were sealed in thin-walled glass capillaries with diameter of 1.5 mm. Experimental diffraction patterns are shown in Fig. 4(a) introduced later on. The diffraction patterns were corrected for experimental artifacts such as background scattering, absorption, Compton scattering and others, normalized in absolute electron units and reduced to so-called structure factors, $S(q)$. The structure factors were then Fourier transformed to atomic pair distribution functions (PDF)s $G(r)$, using the relationship:

$$G(r) = \frac{2}{\pi}\int_{q=0}^{q_{max}} q[S(q) - 1]\sin(qr)\mathrm{d}q, \quad (1)$$

where q_{max} = 25 $Å^{-1}$ in the present experiments. Here q is wave vector defined as $q = 4\pi\sin(\theta)/\lambda$, where θ is half of the angle between the incoming and diffracted synchrotron X-ray beams and λ is the wavelength of the X-rays used. Note, as derived, atomic PDFs $G(r)$ are experimental quantities that oscillate around zero and show positive peaks at real space distances, r, where the local atomic density $\rho(r)$ exceeds the average one ρ_o (see Fig. 4b introduced later on). This behavior can be expressed by the equation $G(r) = 4\pi r\rho_o[\rho(r)/\rho_o - 1]$, which is the formal definition of the PDF $G(r)$.[16–18] High-energy synchrotron XRD and atomic PDFs analysis have proven very efficient in studying the atomic-scale structure of nanometer-size materials, including metallic nanoparticles.[19,20]

In situ scanning tunneling microscopy study was done on a Nanoscope Multimode V Scanning Probe Microscope (Digital Instrument Corp.). A Pt–Ir wire (1 cm, 85 : 15) was etched in 1 : 3 saturated $CaCl_2$ water solution at 30 V AC, then at 8 V AC, to get the STM probe. Then the tip was coated by Apiezon wax and only the very end part of the tip was exposed to electrolyte to minimize the leakage current. A thin Pt wire is used as the counter electrode (CE), Ag/AgCl wire is used as reference electrode (RE). A custom-built Teflon cell was used for the *in situ* electrochemical STM study.

In situ Fourier transform infra-red spectroscopy (*in situ* FTIR) was measured using a NICOLET 6700 FTIR apparatus equipped with a MCT-A detector cooled with liquid nitrogen. The compartments were purged using compressed air free of CO_2 and H_2O at an inlet pressure of 60 psi from a Parker Balston Purge Gas Generator operating at a flow rate of 9 L min^{-1}. The electrode potential was controlled by BAS CV-27 potentiostat. A custom-made spectro-electrochemical Teflon cell with a hemispherical ZnSe window was connected to the optical window (ZnSe) *via* a Teflon tape. An ink made of the electrocatalyst suspended in ultrapure water, isopropanol and nafion was put as a film on a polished Au(100) single-crystal operating as the working electrode (WE), which was placed together with the reference electrode (SCE, +0.323 V *vs.* RHE) and counter electrode (Pt wire) in the cell filled with electrolyte (0.1 M $HClO_4$ + 0.5 M C_2H_5OH). The WE was pushed against the optical window under 0.15 V *vs.* RHE to achieve appreciable increase of interferogram peak-to-peak signal. Afterwards the sample compartment was closed and dry compressed N_2 was purged for two hours to eliminate water and CO_2 from the spectrometer compartment. The background spectrum was collected at 0.15 V and the potential was stepped from 0.2 V by 0.10 V in positive direction to 1.2 V. At each potential, interferograms were collected at 8 cm^{-1} resolution with 128 scans, with 20 seconds of delay between setting (potential switch) and measurements to allow the interface to reach equilibrium.

For CO adsorption studies, the working electrode (WE), inserted into a glass tube, was placed in the cell filled with electrolyte (0.1 M perchloric acid saturated with CO) equipped with the reference electrode (SCE) and counter electrode (Pt wire). Firstly, a potential of 0.2 V was applied and the WE was pushed against the optical window to achieve appreciable increase of interferogram peak-to-peak signal. Then, the sample compartment is closed and dry compressed air is purged for two hours to eliminate water and carbon-dioxide from the environment. During this time the potential was kept on 0.2 V while a CO monolayer remains adsorbed on the electrode surface. After two hours the potential was stepped every 0.1 V in positive direction and at each potential interferogram was collected (at 8 cm^{-1} resolution with 512 scans) with 20 seconds of delay between setting (potential switch) and measurements (interferogram collection) to allow the interface to reach equilibrium. The final sample interferogram was collected at potential of 1.2 V. The background interferogram was collected at a potential (0.9 V) where all adsorbed CO is expected to be oxidized.

The interferograms were processed using OMNIC software to obtain characteristic spectra. Spectra were obtained by Subtractively Normalized Interfacial Fourier Transform Infrared Spectroscopy (SNIFTIRS). During a typical SNIFTIRS, the electrode potential was modulated between values $E1$, sample potential (usually potential for strong adsorption of probe molecules or production of intermediates) and $E2$, background potential (where there is no adsorption of probe molecule). The spectrum is obtained by the equation:

$$\Delta R/R = \{R(E2) - R(E1)\}/R(E1), \quad (2)$$

where, the difference between two single beam reflectivities (R) at applied potentials $E1$ and $E2$, is ratioed to the reflectivity at one of the applied potentials ($E1$). The goal of computing this difference (normalized) spectra is to obtain spectra essentially free from bulk contribution. SNIFTIRS method is part of the external reflection configuration used to study structural aspects of the adsorption processes.[21]

Electrochemical testing were carried out in a three-compartment electrochemical glass cell at room temperature

using a Biologic SP 150 (Biologic) potentiostat. The electrolytes were deaerated with high-purity N_2 gas (99.998% Linde, Germany) before every measurement and during the experiments the N_2 was purged over the electrolyte through the working electrode compartment. A large surface area Pt counter electrode was contained in a separate compartment. A saturated mercury–mercurous sulfate electrode (MMS) was implemented *via* a Luggin capillary in a separate compartment of the experimental setup as reference. All potentials reported here are given in respect to a reversible hydrogen electrode (RHE).

3. Results and discussion

3.1 Electrocatalysts preparation

Supported poly-crystalline Au nanoparticles (Au NPs) with a 40 wt% metal loading on carbon were taken as starting material for the electrodeposition of Pt ML and sML catalysts. The TEM micrograph in Fig. 1(a) shows a mean Au particle size of about 12 nm. Cyclic voltammogram (CV) of the Au nanoparticles in 0.05 M H_2SO_4 electrolyte at a scan rate of 20 mV s^{-1}, displayed in Fig. 1(b), showed the characteristic voltammetric red-ox peak profile of Au, observed between 1.1 V and 1.5 V. A second broader peak observed between 0.5 and 0.6 V can be attributed to sulphate ion adsorption on the surface of gold.

Synthesis of Au@Pt (s)ML catalysts using the SLRR procedure first necessitated an electrochemical cleaning of the Au surface in order to eliminated the effect of any surfactants, followed by controlled Cu ML deposition. The optimal positive potential limit during the cleaning protocol was determined by a series of CVs with varying electrode potential range (Fig. SI.1-a, ESI†). As the potential was swept to a more positive value, the surface Au oxidation peak became more and more distinct. A potential of +1.27 V was chosen as the upper potential limit to avoid extensive Au surface oxidation, while ensuring removal of surface contaminations. Fig. SI. 1-b (ESI†) reports a CV of Au NPs in 0.5 M H_2SO_4 recorded in the custom-made SLRR cell. After the cleaning step, Cu^{2+} was introduced into the cell under deaerated conditions. Fig. SI. 1-b (ESI†). also shows a typical CV of Au NPs in 0.5 M H_2SO_4 + 0.05 M $CuSO_4$ solution with Cu deposition and stripping peak.

During the SLRR the applied electrode potential is held just slightly positive of the reversible Cu^{2+}/Cu bulk potential to avoid bulk deposition and at the same time, ensure a complete overlayer formation. Fig. SI. 1-c (ESI†) shows Cu UPD current transients on the Au NPs in 0.05 M H_2SO_4 + 0.05 M $CuSO_4$

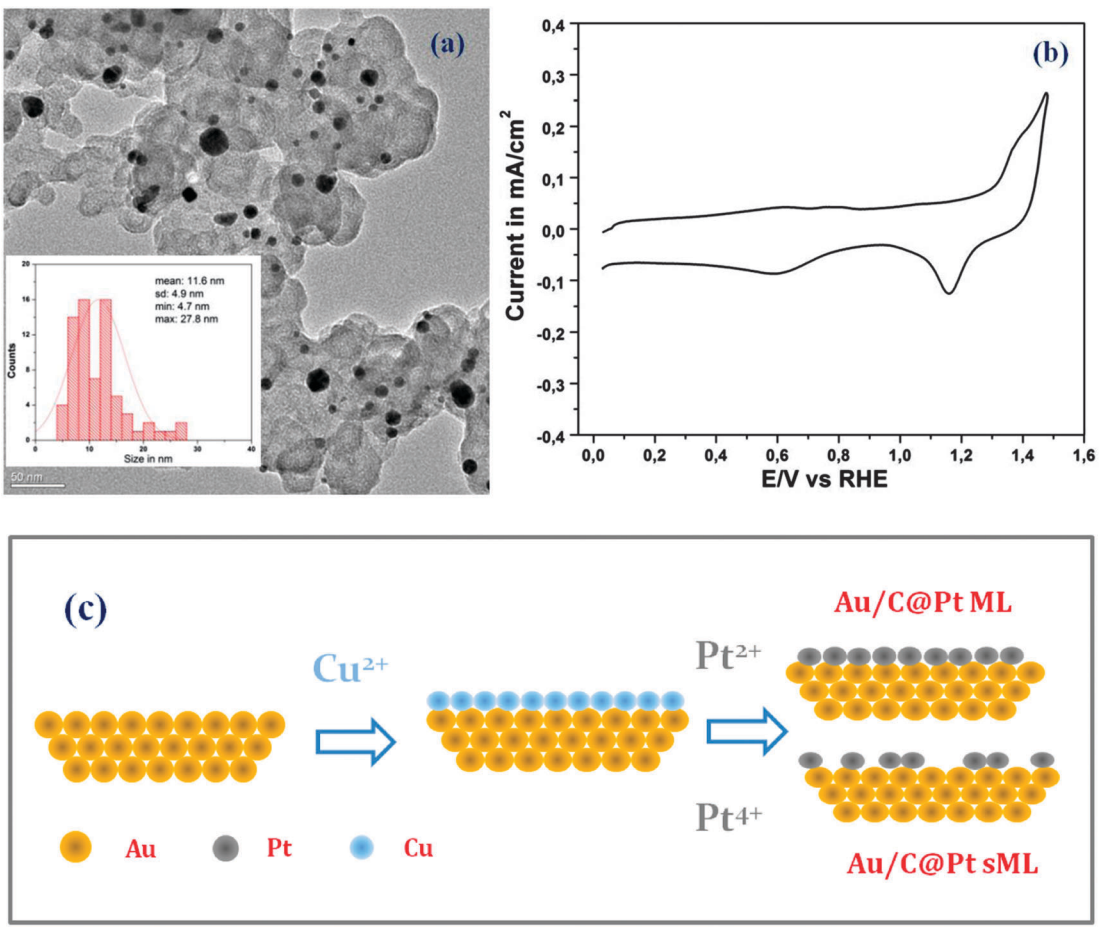

Fig. 1 (a) TEM micrograph of carbon supported Au NPs (40 wt%), inset: size distribution histogram of the Au NPs; (b) cyclic voltammogram of Au NPs in 0.5 M H_2SO_4 at a scan rate of 20 mV s^{-1}; (c) schematic representation of electrochemical synthesis of Au@Pt ML and sML *via* SLRR method.

solution recorded at different potentials ranges. The Au NPs were first conditioned at a constant electrode potential of +0.98 V for 10 seconds. Then the potential was stepped to a Cu UPD potential between +0.52 V and +0.22 V in 0.02 V decrements. At around +0.30 V, a change in the current transient is observed in the diffusion-controlled tail over 70 s. From these results an electrode potential of E = +0.33 V was chosen as the optimized Cu UPD deposition potential on the Au NPs as no evident change in the current is seen around this potential. Anodic stripping of the deposited Cu monolayer at E = +0.98 V subsequently produced a sharp anodic Cu stripping peak (Fig. SI. 1-d, ESI†), which was integrated to confirm the formation of the full Cu monolayer.

A schematic representation of electrochemical synthesis of Au@Pt ML and sML *via* SLRR method is shown in Fig. 1(c). Once an UPD layer of Cu^{2+} was formed on the surface of the Au NPs, Pt^{2+} or Pt^{4+} was introduced into the cell for spontaneous galvanic displacement with the non-noble Cu atoms acting as sacrificial layer forming Au@Pt ML and sML depending on the oxidation states of the replacement Pt ions.

3.2 Physico-chemical characterization of Au@Pt (s)ML catalysts

Electron and scanning probe microscopy. The stoichiometry of SLRR between Cu UPD ML and Pt^{2+} ions suggests the formation of a Pt ML with full coverage of the Au NPs. Fig. 2(a) shows the TEM micrograph of the Au@Pt ML catalyst. High resolution inset shows 2D clusters of Pt atoms covering the entire surface of the Au NPs forming a composite layer. In contrast, the SLRR of Cu UPD ML with Pt^{4+} ions led to the formation of Pt 2D clusters with submonolayer coverage of the Au NPs. Fig. 2(c) shows the TEM micrograph of the Au@Pt sML catalyst with Pt atoms forming clusters which are separated and spread out on the surface of the Au NPs. This is morphologically very similar to what was reported

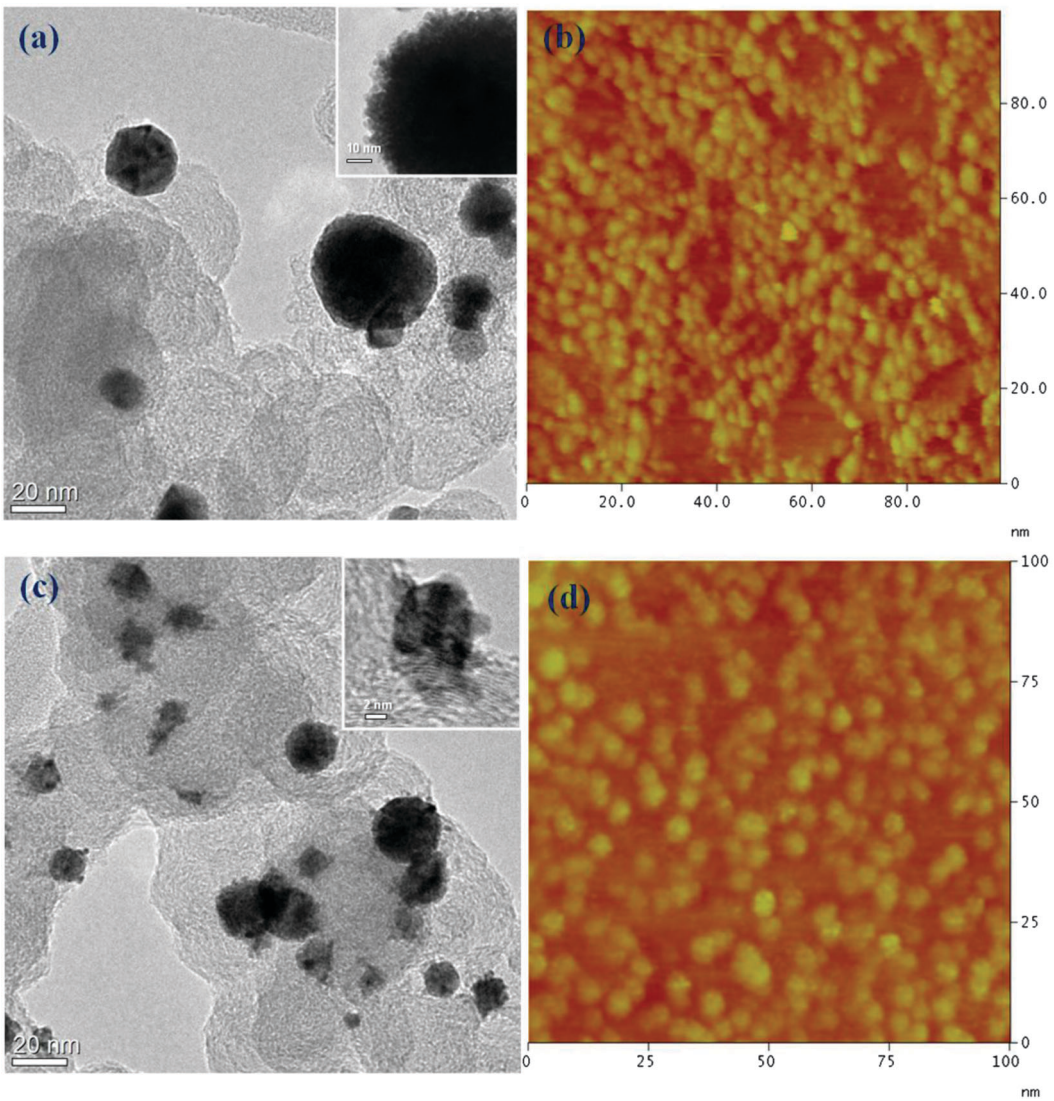

Fig. 2 (a) TEM micrograph of Au@Pt ML, inset: HRTEM of a selected particle showing Pt clusters on surface; (b) STM image of Pt^{2+} deposition by Cu SLRR on Au(111); (c) TEM micrograph of Au@Pt sML, inset: HRTEM of a selected particle; (d) STM image of Pt^{4+} deposition by Cu SLRR on Au(111).

for Pt ML on Pd NPs produced in a comparable scale-up batch reactor synthesis procedure.[15] The morphology of the Pt monolayer or submonolayer is characterized by the size, percentage of coverage and density of the 2D Pt nanocluster constituents.

To determine accurate values for the size and coverage of the Pt 2D clusters on the Au substrates, Pt monolayer model catalysts were prepared using Au(111) single crystal electrodes using SLRR of Cu UPD ML under identical conditions as in the case of Au NPs. Fig. 2 shows STM images of the morphology of the Pt (s) ML clusters deposited on the Au(111) single crystals using Pt^{2+} (Fig. 2(b)) and Pt^{4+} (Fig. 2(d)) ions. The Cu UPD ML was formed in 1 mM Cu^{2+} and 0.05 M H_2SO_4, while the SLRR reaction occurred in a solution of 1 mM Pt^{2+} and 0.05 M H_2SO_4. Fig. SI. 2 (ESI†) shows the particle size and coverage analysis of the STM images of Au@Pt (s)ML catalysts. The Pt coverage after Pt^{2+} SLRR reaction was found to be ~80.0% with a mean cluster size of 2.2 nm^2. The Pt cluster coverage using Pt^{4+} was ~50.0%, which is essentially the theoretically expected value; the experimental mean cluster size now was 2.9 nm^2, hence slightly larger than in case of Pt^{2+}.

From stoichiometric arguments one would ideally expect to see a 2× larger Pt coverage when using the Pt^{2+} ions in the galvanic displacement. The model experiments on single crystal recovered a coverage ratio of 80 : 50 or 1.6. Assuming complete galvanic Pt displacement from the Pt^{4+} salt, the lower-than-ideal experimental ratio may either indicate the formation of 3D Pt clusters or else may be related to a roughly 1.25× larger amount of chloride ions liberated near the interface during the reduction of Pt^{2+} complex as compared to Pt^{4+}. This would promote the stability of Cu^+ as $\{CuCl_2\}^-$ instead of Cu^{2+} and hence would lower the effective Pt monolayer coverage.[10] Important for our argument here is that the displacement using Pt^{2+} and Pt^{4+} resulted in qualitatively different morphologies of the Pt mean cluster size: Pt^{2+} generated a *smaller Pt cluster size*, a result in agreement with recent experimental and theoretical study of the Pt nucleation during SLRR of Cu UPD ML.[12] According to this study, SLRR having Pt in lower oxidation state promotes a larger Pt nucleation density and formation of Pt deposit with overall smaller clusters.

Based on the model experiments, we are now in a position to more accurately interpret the TEM images of the Au@Pt (s)ML catalysts. It can be concluded that Pt^{2+} ion displacement resulted in a composite layer of close-packed Pt nanoclusters. Pt^{4+} ions, in contrast, resulted in more dispersed Pt nanoclusters on the Au surface. The EDS analysis on Au@Pt ML and Au@sML shows that Au : Pt ratio in nanoparticles is 83 : 17 for SLRR with Pt^{2+} while it is 90 : 10 for SLRR with Pt^{4+}. The mutual Au : Pt ratio between these experiments (83 : 17/90 : 10) is close to what was recovered by comparing the Pt coverage in our model experiments (Pt ratio of 17 : 10 = 1.7 which is essentially the coverage ratio we recovered in the model experiments).

Atomic pair distribution function (PDF) analysis. To reveal the 3D atomic ordering in the Au@Pt ML and Au@sML in finer detail, high-energy synchrotron X-ray diffraction experiments coupled with atomic pair distribution function (PDF) analysis were carried out. Experimental high-energy XRD patterns are shown in Fig. 3(a). Peaks in the patterns of the Au NPs, Au@Pt ML and Au@sML catalysts are sharp, reflecting their good crystallinity and large crystallite size. Bragg peaks of comparative patterns of supported pure Pt NPs catalysts are rather broad reflecting the smaller size/poor crystallinity of these particles.

Atomic PDFs extracted from the HE-XRD patterns of Fig. 3(a) are shown in Fig. 3(b). The series of peaks in the PDFs reflect the presence of well-defined atomic coordination spheres in all nanoparticles studied. The series extends to high real-space distances with supported Au NPs, Au@Pt ML and Au@sML nanoparticles reflecting their good crystallinity. Peaks in the PDF for supported Pt NPs decay to zero at much shorter real-space distances reflecting the poor degree of crystallinity and smaller size of these nanoparticles. All experimental PDFs were fit with structure modes based on fcc-type structure. Fits are of very good quality confirming the single phase state all nanoparticles studied. The refined fcc-lattice parameters, denoted as "a", are given for each catalyst in Fig. 3(b).

Lattice parameters for supported Au NPs and supported Pt NPs nanoparticles are close to those of bulk Au (4.078 Å) and bulk Pt (3.92 Å). The lattice parameter of Au@Pt sML does not deviate substantially from that of supported Au NPs nanoparticles indicating negligible interaction between supported Au NPs core and Pt sML deposited on it. The lattice parameter of Au@Pt ML, however, appears shorter than that in supported

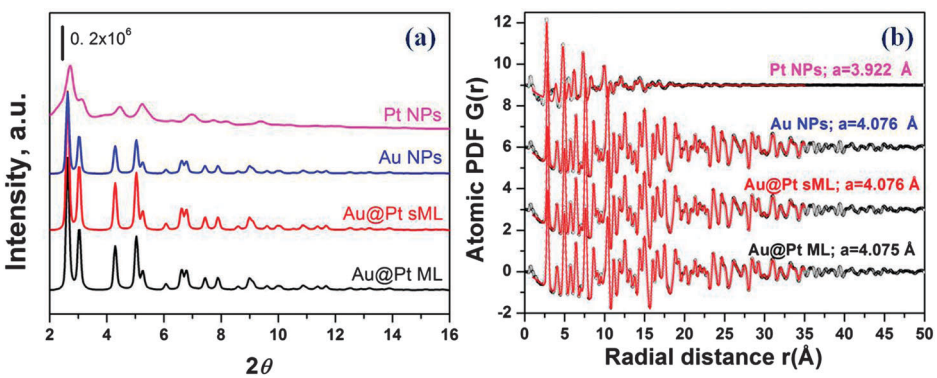

Fig. 3 (a) Experimental HR-XRD patterns (λ = 0.1080 Å); (b) fits (lines in color) to the experimental (black symbols) atomic PDFs indicate a fcc-type structure.

Au NPs particles indicating the presence of non-negligible interaction between supported Au NPs core and Pt ML deposited on it. The absence and presence of interaction between supported Au NPs core and Pt layer deposited on it in Au@Pt sML and Au@Pt ML nanoparticles may be expected since the coverage of the surface of supported Au NPs seeds is much larger in the latter (~80%) than in the former (~50%).

3.3 *In situ* FTIR spectroscopic studies of Pt (s)ML catalysts

In situ spectroscopic investigations of reactive intermediates during the EOR on the Pt (s)ML electrocatalysts were carried out to the study mechanistic aspects, in particular, to check whether the catalysts support the direct C–C bond splitting reflected by the complete oxidation of ethanol to carbon dioxide. Fig. 4, 5 and 6 show the SNIFTIRS spectra of *in situ* ethanol oxidation and the intermediates produced during the experiment for Au@Pt ML, Au@Pt sML and supported Pt NPs, respectively.

Au@Pt ML. In Fig. 4(a), in *situ* FTIR spectra during ethanol oxidation of Au@Pt ML in a potential range of 0.2 V to 1.2 V is shown. Onset of CO_2 evolution at around 2300 cm^{-1} frequency is observed as early as E_{onset} = +0.3 V implying efficient C–C bond splitting at low overpotential. The area under the typical CO_2 stretching peak increased with increase in electrode potential. Other IR active peaks were assigned as follows: peak/band located around 1700 cm^{-1} for the CO stretching mode of acetic acid and acetaldehyde; band at 1280 cm^{-1} marks the C–O stretching in acetic acid; at 1350–1410 cm^{-1} for the CH_3 in-plane bending mode and O–C–O stretching of adsorbed acetate; finally, the 900 cm^{-1} band is associated with the C–C–O asymmetric stretching of acetaldehyde while the broad band at 1100 cm^{-1} stems from ClO_4^-. Observation of characteristic acetic acid and acetaldehyde peaks suggested the coexistence of partial-oxidation pathways.

In addition to the linear sweep voltammetry, chronoamperometric studies at a constant applied electrode potential were performed to follow the evolution of the CO_2 peak. For instance, the time evolution of *in situ* FTIR spectra during ethanol oxidation at a constant electrode potential of E = + 1.2 V is shown in Fig. 4(b). Spectra were recorded every 10 min for 1 hour. Initially, there was a prominent CO_2 peak which gradually diminished with time due to local ethanol depletion implying that the EOR kinetics are quite fast compared to the ethanol diffusional transport inside the ATR-thin electrolyte film configuration. The electrode potential was high enough to drive the oxidation reaction of ethanol molecules to completion.

Au@Pt sML. *In situ* FTIR spectroscopic results obtained for the Au@Pt sML catalysts were markedly different from the catalyst with the full Pt monolayers (Fig. 5). This suggests that the morphology of Pt monolayer island clusters plays an important role for their surface catalytic properties. Most prominently, the CO_2 stretching mode for of Au@Pt sML emerges at much more positive electrode potentials of E_{onset} = +0.7 V compared to Au@Pt ML (E_{onset} = +0.3 V) indicating less efficient C–C bond splitting and oxidation. Chronoamperometric studies at a constant applied electrode potential of E = +0.8 V is shown in Fig. 5(b). The CO_2 peak increases from 0 min to 10 min and then gradually decreases with time. It can be noted that at this potential, CO_2 evolution is still seen at the 60 min mark indicating that some ethanol molecules are still adsorbed on catalysts surface at this point in time and available for oxidation.

The observation of CO_2 evolution in both the case of Au@Pt ML and Au@Pt sML is highly significant as past studies on Pt ML on Au(111) single crystal surfaces had yielded no CO_2 during *in situ* FTIR analysis.[13] C–C bond splitting during EOR was not observed before in such types of electrocatalysts.

An important mechanistic observation is the appreciable detection of the C═O stretching band related to acetaldehyde and acetic acid (1700 cm^{-1}) appears at more positive potentials than the first detection of the O═C═O solution stretching band (2300 cm^{-1}) for both catalysts. However, in the Au@Pt ML case, the difference between first detection potential for the

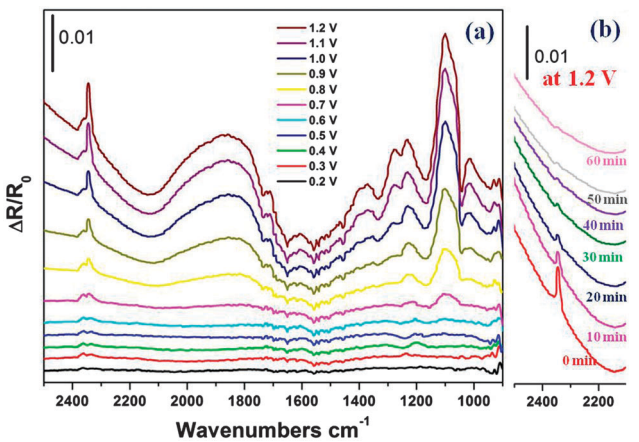

Fig. 4 (a) *In situ* SNIFTIRS spectra of ethanol oxidation of Au@Pt ML at a potential range of 0.2 V to 1.2 V *vs.* RHE in 0.1 M $HClO_4$ + 0.1 M CH_3CH_2OH. Spectrum at 0.15 V is used as background; (b) spectra of ethanol oxidation over time at a constant potential of +1.2 V at the CO_2 evolution region.

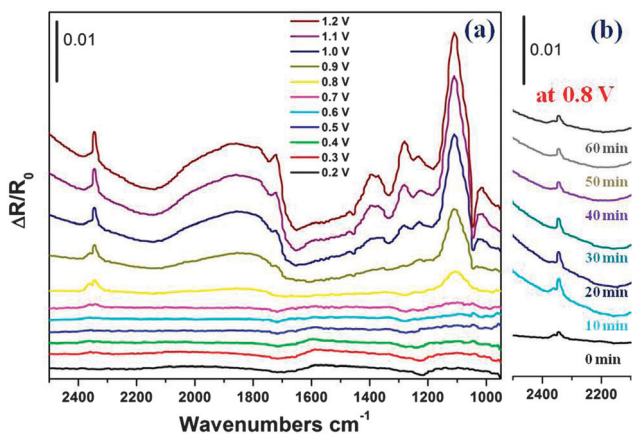

Fig. 5 (a) SNIFTIRS spectra of ethanol oxidation of Au@Pt sML at a potential range of 0.2 V to 1.2 V *vs.* RHE in 0.1 M $HClO_4$ + 0.1 M CH_3CH_2OH. Spectrum at 0.15 V is used as background. (b) Spectra of ethanol oxidation over time at a constant potential of 0.8 V at the CO_2 evolution region.

CO_2 and C═O related to acetaldehyde/acetic acid is quite larger as compared to Au@Pt sML. It appears that over the entire potential range between +0.3 V to +0.7 V the ethanol oxidation on Au@Pt ML proceeds according the 12-electron complete oxidation pathway with the C–C bond splitting step occurring for the adsorbed ethanol molecule, not the partially oxidized products. Above electrode potentials of +0.7 V, the mechanistic reaction pathway branches off towards aldehyde and acetic acid. In the case of Au@Pt sML, the potential window where this occurs is much narrower, roughly +0.7 V to +0.8 V.

Based on the lattice mismatch between Pt and Au, we expect some tensile strain in both Au@Pt ML and Au@Pt sML. As a result of this, the Pt d-band center positions of the two catalysts is upshifted to different degrees toward the Fermi level, resulting in distinct chemisorption and bond breaking reactivity. This means that they bind intermediates stronger and should show enhanced reactivity as compared to Pt nanoparticles of comparable size.[12] To corroborate this, we compared SNIFTIR spectra of these two catalysts during ethanol oxidation with those obtained for supported Pt NP reference catalysts, Fig. 6. As one can see, the *in situ* SNIFTIR spectra of Pt NPs show emergence of CO_2 stretching bands at more positive electrode potentials compared to Au@Pt ML (+0.7 V *vs.* +0.3 V), at potentials comparable to Au@Pt sML. The emergence of the C═O stretching band (1700 cm^{-1}) associated with acetaldehyde/acetic acid species occurs at a similar electrode potential as the CO_2 stretching band (~+0.7 V). However, the peak area ratio between the C═O peak and the CO_2 peak is much larger for Pt NPs compared to the Pt (s)ML catalysts. Chronoamperometric studies at a constant applied electrode potential of E = +1.2 V is shown in Fig. 6(b). The CO_2 peak is found to gradually decrease with time and some evolution is still seen at the 60 min mark similar to what was onserved for Pt sML.

From this analysis, it appears that tensile strain in Pt ML and sML on Au nanoparticles does promote the C–C bond splitting and enhances the selectivity towards the complete 12 electron ethanol oxidation.

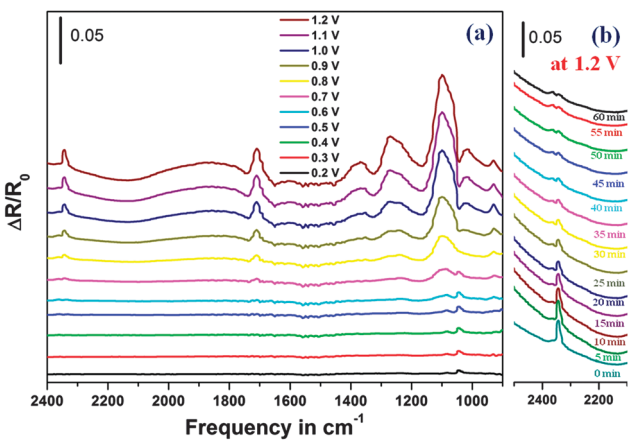

Fig. 6 (a) *In situ* SNIFTIRS spectra of ethanol oxidation of supported Pt NPs at a potential range of 0.2 V to 1.2 V *vs.* RHE in 0.1 M $HClO_4$ + 0.1 M CH_3CH_2OH. Spectrum at 0.15 V is used as background. (b) Spectra of ethanol oxidation over time at a constant potential of 1.2 V at the CO_2 evolution region.

In the absence of any morphological difference, Au@Pt ML is expected to have larger tensile stain than Au@Pt sML. To correlate the observed C–C bond splitting and CO_2 formation activity difference with the structural and morphological differences of the catalysts, we recall our earlier conclusion that the Au@Pt ML catalyst morphology consists of a composite layer of contiguous 2D Pt nanoclusters compared to an isolated island structure made up of larger 2D Pt clusters for the Au@Pt sML catalyst. These two morphologies have significant presence of size-dependent strain due to the presence of sub-coordination around the perimeter of these clusters, which results in compressive component of the strain. This phenomenon has been previously addressed in detail for Pt-submonolayer on Au(111) system studying its activity for HOR.[22] Both, continuum elasticity and DFT calculations has shown that active strain in Pt nanoclusters has strong radial dependence. The average strain in Pt nanoclusters was found to be always smaller than the strain set by epitaxial relation between Pt and Au(111) due to the finite size effect. The smaller Pt nanoclusters experience a larger finite size effect and they were found less active for HOR. Recent reports also indicate that finite size effect has strong influence on Pt-submonolayer on Au(111) electrosorption behavior.[12] Again, smaller Pt nanoclusters were found to have weaker bond with CO as compared to larger ones. Therefore, in agreement with these studies, we conclude that in our case, smaller Pt cluster size in Au@Pt ML leads to a larger compressive size dependent strain which works against the expansive epitaxial strain. Hence a sML surface coverage with larger Pt cluster size (less compressive strain) in Au@Pt sML is expected to have more *resultant overall* tensile strain.

Any shift in the Fermi level can be detected indirectly by studying the interaction of the d-orbitals of Pt with carbon monoxide. CO is an excellent probe to study this change due to its back bonding with Pt. The vibrational frequency of CO, ν_{CO} will change with any upward or downward shift of the Fermi level. Fig. SI. 3 (ESI†) shows the SNIFTIRS spectra recorded for Au@Pt ML (a) and Au@Pt sML (b) during CO adsorption. The CO adsorption frequency on catalysts surface is recorded with change in electrode potential. Characteristic infrared wavenumbers (frequencies) (~2090–2040 cm^{-1}) corresponding to linearly adsorbed CO in saturated acid solution were observed. The variation of the wavenumber maximum with applied potential is due to Stark effect. Firstly, for each spectra, an increase of frequency *i.e.*, increase of C–O bond strength at lower potentials is observed. Then, at higher potentials the decrease of frequency and a shift to smaller wavenumbers occurs due to coverage dependence and anion co-adsorption. At certain potentials CO oxidation starts which leads to phase transformation of the remaining CO giving adequate response in the frequency of the band maximum. Furthermore, by increasing the potential, the CO will be totally oxidized and no spectra will be observed with SNIFTIRS.

Comparing the FTIR fingerprints of adsorbed CO at +0.22 V for ML and sML catalysts, it is seen that both catalysts show

their CO stretching mode at a much lower wavenumbers (Au@Pt ML: 2055 cm^{-1} and Au@Pt sML: 2045 cm^{-1}) compared to bulk Pt (2078 cm^{-1}). A lower CO vibrational frequency translates to stronger Pt–C bond and weaker C═O bond due to upshift of the d-band center towards the Fermi level. Hence, bulk Pt was found to have weaker Pt–C bond as compared to both the Au@Pt ML and Au@Pt sML catalyst. Because of the general tensile Pt strain in both catalysts due to the lattice mismatch between Pt and Au, an upshift in d-band center can be inferred for both catalysts as compared to bulk Pt that shows a blue-shifted higher CO stretching wavenumbers by $\sim$30 cm^{-1}. The slightly lower ν_{CO} in Pt sML (by $\sim$10 cm^{-1}), as compared to Pt ML indicates a larger upshift in d-band center for this catalyst. From these results, surface chemisorption of carbonous fragments is expected to be stronger on Au@Pt sML than on Au@Pt ML. Linking these insights in the chemisorption of the two bimetallic catalysts and pure Pt to the their ability to split the C–C bond and form CO_2, we conclude that increasing tensile strain is beneficial for C–C bond splitting (transition from pure Pt to Au@Pt ML), however, that further increase of tensile strain (going from Au@Pt ML to Au@Pt sML) is detrimental to an efficient C–C bond splitting. This is likely because molecular fragments then adsorb too strongly and make active sites inaccessible. The effect of the two distinct Pt layer morphologies and their amount of tensile strain on their surface chemisorption and EOR activity is schematically shown in Fig. 7.

Overall, we can conclude that the morphology of the Pt layers on the Au nanoparticle plays a very significant role in catalyst selectivity and activity during the ethanol oxidation reaction. However, SNIFTIR data also indicate that the smaller Pt cluster morphology in Pt ML provides optimal catalytic C–C bond splitting selectivity, making it more conducive for complete ethanol oxidation to CO_2. It is evident that the behavior of Pt ML catalysts is sensitively dependent on the Pt cluster morphology, which needs to be appreciated when considering experimental conditions and procedures for their synthesis.[13]

3.4 Electrocatalytic ethanol oxidation reactivity of Au@Pt (s)ML

Electrochemical studies were performed for Au@Pt ML and Au@Pt sML electrocatalysts after their synthesis *via* SLRR of Cu UPD ML. Hydrogen UPD curves (Fig. SI. 4-a, ESI†) was recorded in deaerated 0.5 M H_2SO_4 at 50 mV s^{-1} in the potential range of 0.05 V to 1.0 V confirming the presence of Pt on the surface of the supported Au NPs. Distinctive features of Pt UPD region is observed in both Au@Pt ML and Au@Pt sML. Pt coverage is understandably more prominent in the Pt monolayer than in the sub-monolayer configuration/morphology. This observation is confirmed by CO stripping curves (Fig. SI. 4-b, ESI†) where the Pt ML shows significant CO stripping area compared to the Pt sML.

Fig. 8 shows the forward scans of EOR curves of Au@Pt ML and Au@Pt sML at scan rate of 10 mV s^{-1} in deaerated 0.5 M H_2SO_4 + 1 M C_2H_5OH at both room temperature (RT) and fuel cell working temperature of 60 °C. Catalyst loading was controlled at 153 μg cm^{-2} for all catalysts and current density was corrected for Pt surface active area. Sluggish reaction kinetics is observed with delayed on-set in case of the ethanol oxidation in room temperature. At 60 °C, the kinetics of the reaction is observed to be much faster with a more negative shift in the on-set potential ($\sim$0.35 V similar to what was observed in the FTIR). At 0.7 V *vs.* RHE, current density was found to be 5.6 mA cm^{-2} for Au@Pt ML and 2.1 mA cm^{-2} for Au@Pt sML. These current densities obtained compared quite favorably with what is reported in literature[13] at around 0.7 V where substantial oxidation is observed. The results showed that Au@Pt ML had significantly higher activity towards EOR than Au@Pt sML which is in agreement with time dependent IR

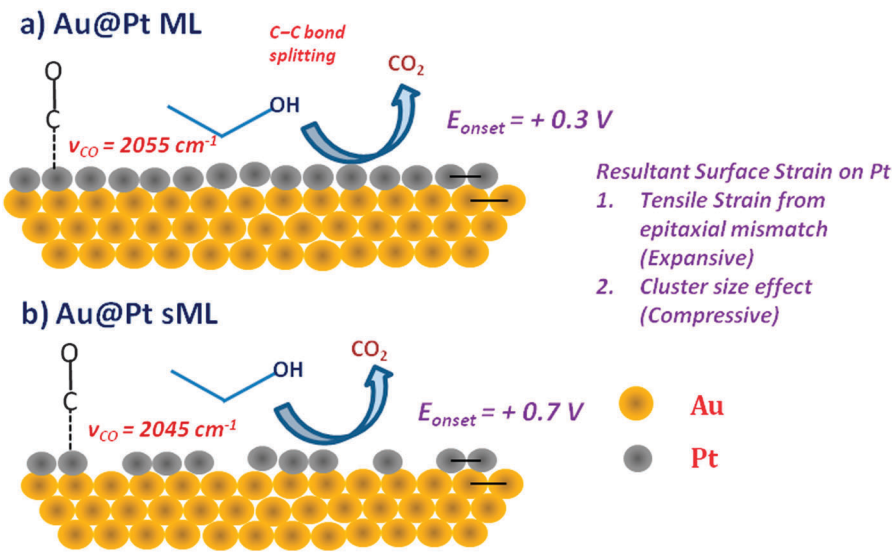

Fig. 7 Illustration of the Pt layer morphology of Au@Pt ML and Au@Pt sML electrocatalysts and their effect on vibrational modes of CO probe molecules and onset potential for C–C bond splitting and CO_2 formation from ethanol.

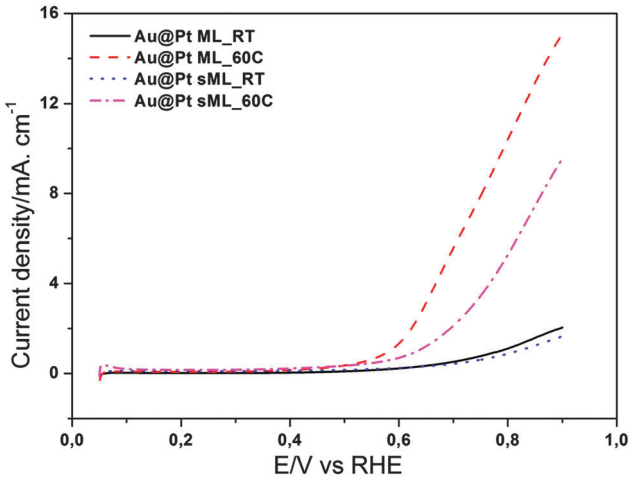

Fig. 8 EOR comparison curves of Au@Pt ML at room temperature (RT), Au@Pt ML at 60 °C, Au@Pt sML at room temperature (RT), Au@Pt sML at 60 °C, at 10 mV s^{-1} in deaerated 0.5 M H_2SO_4 + 1 M C_2H_5OH. Catalyst loading: 153 μg cm^{-2} and current density is corrected for Pt surface active area. Geometric area of the GC electrode (0.196 cm^2).

study (Fig. 4–6) showing much shorter time for establishment of transport limitation in the case of Au@Pt ML than in the case of Au@Pt sML and supported Pt NPs.

The electrochemical results are consistent with SNIFTIR data. The catalyst morphology that has smaller Pt nanoclusters and, therefore, less tensile strain appears as the one having faster kinetics for EOR. Considering a d-band model to interpret catalyst activity[14] more tensile strain in catalysts during simple reactions such as HOR, should lead to stronger interaction and adsorption of the reactant on the catalyst surface and direct improvement of the catalyst activity.[22,23] However, in the case of EOR with complex reaction pathway possibilities, a more positive strain and larger shift in d-band center towards Fermi level means also a stronger adsorption of intermediates. Therefore, the benefit of increasing reactivity of catalyst surface is a matter of an optimum level at which a desired reaction pathway is favored. In our case, most likely a strong ethanol/intermediates adsorption should not compromise the adsorption of water molecules necessary for complete ethanol oxidation to CO_2.[24] Our data suggests that small increase in catalyst reactivity through the introduction of the size dependent strain in 2D Pt nanoclusters is beneficial allowing the oxidation of ethanol to CO_2 at very low potentials (Au@Pt ML). However, further increase in Pt reactivity through the larger Pt nanoclusters (Au@Pt sML) and more tensile strain leads to drop of the EOR rate because of the excessively strong bonding of the reactants and intermediates to the catalyst surface.

4. Conclusions

Supported Au nanoparticles with Pt monolayer and sub-monolayer were successfully synthesized using a SLRR of Cu UPD ML. Various characterization techniques confirmed the presence of Pt on the surface of the Au nanoparticles. HRTEM analysis of the Au@Pt sML and Au@Pt ML showed distinct morphologies of 2D Pt deposit. The model experiments for Pt deposition *via* SLRR of Cu UPD ML on Au(111) having Pt^{2+} and/or Pt^{4+} in reaction solution was confirmed to produce Pt 2D deposit with different morphology in terms of the mean size of their Pt nanocluster population. The C–C bond splitting is observed on the surface of Au@Pt sML and Au@Pt ML electrocatalysts for the first time with the formation of CO_2 during the EOR. The Au@Pt ML catalyst with a balanced overall tensile strain in its Pt overlayer showed a significantly higher catalytic activity C–C bond breaking, the overall EOR and selective generation of CO_2 at low electrode potentials compared to Au@Pt sML with its excessive tensile strain. This work shows that the Au-supported Pt ML morphology has a significant effect on its catalytic behavior. The study highlights the existence of previously unexplored experimentally accessible control parameters such as the Pt layer size and coverage to optimize the catalytic activity in EOR. Further studies are being carried out for application of these Au@Pt sML and Au@Pt ML electrocatalysts in intermediate temperature direct ethanol fuel cells.

Acknowledgements

This project received funds from the "TU9 Sino-German Network for Electromobility" funded by the German Federal Ministry of Education and Research (BMBF) under the project reference number 16N11929. Responsibility for the contents of this publication lies with the author. Work at APS is supported by US-DOE under Contract No. DE-AC02-06CH11357. S. R. Brankovic and Q. Yuan acknowledge the support of NSF CAREER program no. 0955922.

References

1 E. Antolini, *J. Power Sources*, 2007, **170**, 1–12.
2 S. Koh, M. F. Toney and P. Strasser, *Electrochim. Acta*, 2007, **52**, 2765.
3 K. Sasaki, H. Naohara, Y. Cai, Y. M. Choi, P. Liu, M. B. Vukmirovic, J. X. Wang and R. R. Adzic, *Angew. Chem., Int. Ed.*, 2010, **49**, 8602–8607.
4 S. Knupp, M. Vukmirovic, P. Haldar, J. Herron, M. Mavrikakis and R. Adzic, *Electrocatalysis*, 2010, **1**, 213–223.
5 C. Cui, L. Gan, H.-H. Li, S.-H. Yu, M. Heggen and P. Strasser, *Nano Lett.*, 2012, **12**, 5885–5889.
6 R. Loukrakpam, P. Chang, J. Luo, B. Fang, D. Mott, I.-T. Bae, H. R. Naslund, M. H. Engelhard and C.-J. Zhong, *Chem. Commun.*, 2010, **46**, 7184–7186.
7 R. Loukrakpam, J. Luo, T. He, Y. Chen, Z. Xu, P. N. Njoki, B. N. Wanjala, B. Fang, D. Mott and J. Yin, *J. Phys. Chem. C*, 2011, **115**, 1682.
8 R. Loukrakpam, B. N. Wanjala, J. Yin, B. Fang, J. Luo, M. Shao, L. Protsailo, T. Kawamura, Y. Chen and V. Petkov, *ACS Catal.*, 2011, **1**, 562.
9 S. R. Brankovic, J. X. Wang and R. R. Adžić, *Surf. Sci.*, 2001, **474**, L173–L179.

10 D. Gokcen, S.-E. Bae and S. R. Brankovic, *J. Electrochem. Soc.*, 2010, **157**, D582–D587.
11 D. Gokcen, S.-E. Bae and S. R. Brankovic, *Electrochim. Acta*, 2011, **56**, 5545–5553.
12 D. Gokcen, Q. Yuan and S. R. Brankovic, *J. Electrochem. Soc.*, 2014, **161**, D3051–D3056.
13 M. Li, P. Liu and R. R. Adzic, *J. Phys. Chem. Lett.*, 2012, **3**, 3480–3485.
14 T. Bligaard and J. K. Nørskov, *Electrochim. Acta*, 2007, **52**, 5512–5516.
15 K. Sasaki, J. X. Wang, H. Naohara, N. Marinkovic, K. More, H. Inada and R. R. Adzic, *Electrochim. Acta*, 2010, **55**, 2645–2652.
16 T. Egami and S. J. L. Billinge, *Underneath the Braggs' Peak*, 2003.
17 V. Petkov, *Mater. Today*, 2008, **11**, 28–38.
18 V. Petkov, *Synchrotron Radiat. News*, 2009, **22**, 29.
19 R. Loukrakpam, S. Shan, V. Petkov, L. Yang, J. Luo and C.-J. Zhong, *J. Phys. Chem. C*, 2013, **117**, 20715–20721.
20 V. Petkov, B. N. Wanjala, R. Loukrakpam, J. Luo, L. Yang, C.-J. Zhong and S. Shastri, *Nano Lett.*, 2012, **12**, 4289–4299.
21 B. Pettinger, J. Lipkowski and M. Hoon-Khosla, *J. Electroanal. Chem.*, 2001, **500**, 471–478.
22 S.-E. Bae, D. Gokcen, P. Liu, P. Mohammadi and S. Brankovic, *Electrocatalysis*, 2012, **3**, 203–210.
23 L. A. Kibler, A. M. El-Aziz, R. Hoyer and D. M. Kolb, *Angew. Chem., Int. Ed.*, 2005, **44**, 2080–2084.
24 F. Vigier, C. Coutanceau, F. Hahn, E. M. Belgsir and C. Lamy, *J. Electroanal. Chem.*, 2004, **563**, 81–89.